Surface Chemistry Architecture of Silica Nanoparticles Determine the Efficiency of *in Vivo* Fluorescence Lymph Node Mapping

Marion Helle,[†,‡,§,∥,*] Enrico Rampazzo,[⊥,∥] Morgane Monchanin,[†,‡,§] Frédéric Marchal,[†,‡,§] François Guillemin,[†,‡,§] Sara Bonacchi,[⊥] Francesca Salis,[⊥] Luca Prodi,[⊥,*] and Lina Bezdetnaya[†,‡,§]

[†]Centre de Recherche en Automatique de Nancy (CRAN), Université de Lorraine, UMR 7039, Campus Sciences, BP 70239, 54506 Vandoeuvre-lès-Nancy Cedex, France, [‡]CNRS, Centre de Recherche en Automatique de Nancy (CRAN), UMR 7039, Campus Sciences, BP 70239, 54506 Vandoeuvre-lès-Nancy Cedex, France, [§]Research Unit, Institut de Cancérologie de Lorraine, Avenue de Bourgogne, 54511 Vandoeuvre-lès-Nancy, France, and [⊥]Department of Chemistry "G. Ciamician", University of Bologna, Via Selmi 2, 40126 Bologna, Italy. [∥]M. Helle and E. Rampazzo contributed equally to this work.

ABSTRACT

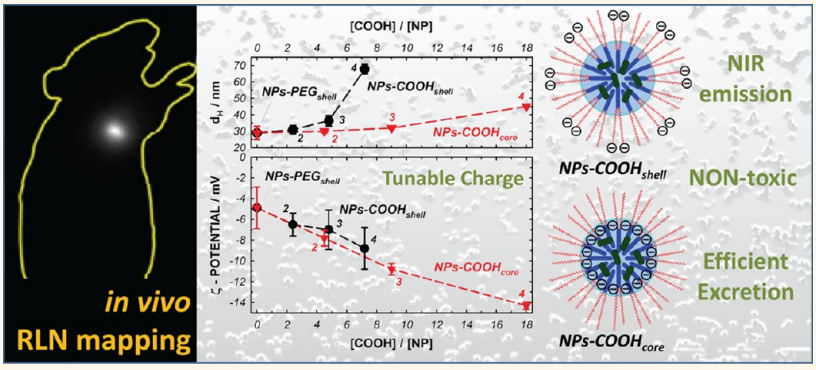

Near-infrared (NIR) imaging of the lymphatic system offers a sensitive, versatile, and accurate lymph node mapping to locate the first, potentially metastatic, draining nodes in the operating room. Many luminescent nanoprobes have received great attention in this field, and the design of nontoxic and bright nanosystems is of crucial importance. Fluorescent NIR-emitting dye doped silica nanoparticles represent valuable platforms to fulfill these scopes, providing sufficient brightness, resistance to photobleaching, and hydrophilic nontoxic materials. Here, we synthesized these highly stable core—shell nanoparticles with a programmable surface charge positioning and determined the effect of these physicochemical properties on their *in vivo* behavior. In addition, we characterized their fluorescence kinetic profile in the right axillary lymph node (RALN) mapping. We found that nanoparticles with negative charges hidden by a PEG shell are more appropriate than those with external negative charges in the mapping of lymph nodes. We also demonstrated the efficient excretion of these nanostructures by the hepatobiliary route and their nontoxicity in mice up to 3 months postinjection. These results indicate the potential future development of these fluorescent nanosystems for LN mapping.

KEYWORDS: silica nanoparticles · NIR fluorescence · hepatobiliary excretion · biodistribution · toxicity · lymph nodes

Noninvasive fluorescence imaging is a powerful tool in the biomedical field. In recent years, its applications have been extended to preclinical *in vivo* imaging as lymphatic mapping,[1] cell tracking,[2] and vasculature[3] or cancer imaging,[4] also with near-infrared (NIR)-fluorescent nanoparticles (NPs) with optimal core—shell architecture.[5−9] In this context, the diagnostic potential of NP-based NIR contrast agents is particularly appreciated considering the deep tissue penetration of NIR radiation and the minimal induced tissue autofluorescence.[10]

Several NIR emitting tracers, such as indocyanine green (ICG),[11] Patent Blue V,[12] silicon dots,[13] or quantum dots,[14] have already been used as lymphatic tracers for sentinel lymph node (SLN) detection in preclinical models. However, many properties such as size, architecture, and toxicity of

* Address correspondence to marion.helle@live.fr; luca.prodi@unibo.it.

Received for review June 3, 2013 and accepted September 24, 2013.

Published online September 24, 2013
10.1021/nn402792a

these tracers are not appropriate and need to be improved. In the case of ICG or Patent Blue V, the main limitation arises from the molecular size of these probes, where they can accumulate into nonsentinel lymph nodes.[15] Recently, Cd-free NIR-emitting quantum dots (QD)[16] demonstrated a good capacity to visualize *in situ* axillary lymph nodes in mice;[17] however their excretion rates from the body were low, and therefore their potential risk for human health cannot be excluded.

Fluorescent dye encapsulation into silica is an interesting alternative since this matrix is inert, biocompatible, nonantigenic, and optically transparent and protects the fluorophores from interactions with the biological environment.[8,18,19] The versatility of silica NPs was exploited by several research groups, who developed sophisticated systems for bioimaging,[7] photodynamic therapy,[20] and cancer cell and bacteria detection.[21,22] Several studies also focused on the proper design of silica NPs to avoid their accumulation *in vivo*[18,23] and, as such, rendering possible optimal theranostic applications.[24] Silica is generally recognized as "safe" by the U.S. Food and Drug Administration, but the toxicity of silica NPs should be questioned since the tiny dimensions of the nanoparticles result in different properties compared to bulk material. Therefore, the biocompatibility of these NPs has to be studied *in vitro* and *in vivo* before any administration.

The main objective of the present paper was to investigate the suitability of cyanine 7 (Cy7)-doped silica NPs as lymphatic tracers for intraoperative fluorescence-guided regional lymph node mapping. With this aim, we synthesized two families of NIR-emitting NPs with a core–shell silica-PEG architecture that differs in terms of charge position. The possibility of controlling the position of the charges inside the nanostructure with a programmable scheme plays a key role in determining the colloidal behavior of nanoparticles. In particular, we found that when the negative charges in the NPs are hidden by the PEG shell instead of being positioned on its surface, the system is more effective in the mapping of right axillary lymph nodes (RALN). We also demonstrate the nontoxicity in mice of these nanostructures, together with their efficient excretion by the hepatobiliary route. All these results could serve as valuable indications for future development of fluorescence-guided nanosystems for lymph node mapping.

RESULTS AND DISCUSSION

Synthesis and Characterization of Nanoparticles. *In vivo* fluorescence-based lymph node mapping requires NPs with efficient absorption and emission in the NIR region along with high colloidal stability in serum, negative ζ-potential, and a diameter in the 20–80 nm range.[25] To fulfill all these requirements, we synthesized two families of Pluronic-based core–shell silica-PEG NPs, with an extremely versatile and reliable synthetic strategy that provides stable and monodisperse NP suspensions with an affordable one-pot procedure.

The possibility of varying the ζ-potential of the particles and their surface charge positioning scheme was obtained in two ways: first we used coaggregates of Pluronic F127 and modified Pluronic F127-COOH[26] as templates to obtain a set of NPs (NPs-$COOH_{shell}$) with variable amounts of negative charge at the periphery of the particles (Scheme 1A), using tetraethyl orthosilicate (TEOS) as the silica precursor. In a second set of particles (NPs-$COOH_{core}$) we exploited the presence of some degree of mesoporosity on the silica core[27] of preformed NPs to obtain negative charge insertion through silica core functionalization using a suitable silane reagent such as CETS (carboxyethylsilanetriol sodium salt, Scheme 1B). Because of its short spacer, the use of CETS provides NPs in which the negative charges were hidden by the PEG shell surrounding the silica core. Both NPs-$COOH_{core}$ and NPs-$COOH_{shell}$ families have been prepared using different amounts of carboxylic groups to modulate their surface properties. It has to be underlined that the NPs-$COOH_{shell}$ family should however present a F127-COOH substitution of the overall surfactant moieties lower than 50%, since a higher substitution degree alters the aggregation properties of the Pluronic F127/Pluronic F127-COOH coaggregates and does not lead to the formation of stable NPs.

The NPs were doped with the cyanine 7 dye (**C**, Scheme 1 and S1 and S2), a derivative of the laser dye IR813 presenting a trialkoxysilane group for covalent linking to the silica matrix. Water-insoluble cyanine 7 dyes are bright NIR-emitting fluorophores and can be considered good candidates as nanoparticle doping material for NIR imaging. Compared to ICG, which bears two sulfonate negative charges, silica encapsulation of **C** is in fact easier because of the absence of electrostatic repulsions between the dye and the negative silanoate groups of silica.[28] **C** possesses a high absorption coefficient with relatively high fluorescent quantum yields in the 800–900 nm range (see Table 1). The position of the absorption and emission maxima for free IR813 and both families of NPs are almost identical (see Table 1 and Figure 1), with a very small red-shift on going from the free IR813 dye to NPs. This behavior is expected since the silica matrix does not typically have a large effect on the photophysical properties of dyes whose excited state does not have a charge transfer character. In all cases the overall brightness of the nanoparticles is higher than that of **C**, mostly because of a strong increase in absorption coefficient due to the multichromophoric nature of these NPs. In addition, the fluorescence quantum yield of the fluorophore is not affected by its encapsulation, suggesting the absence of self-quenching processes at this doping regime.

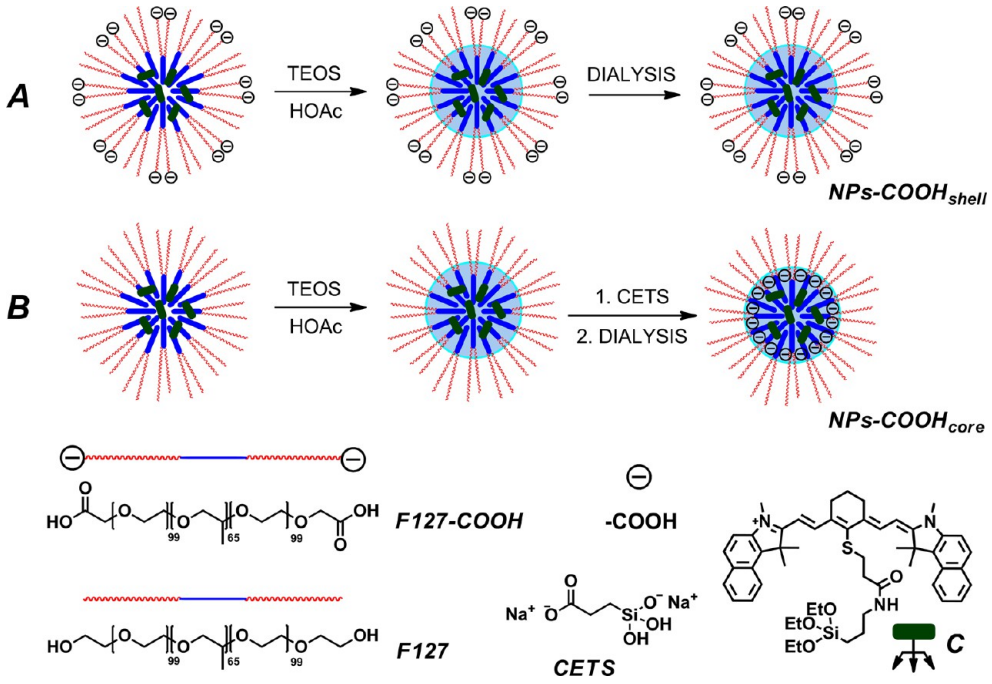

Scheme 1. Synthetic procedure schematization and main components used during the synthesis of NPs-COOH nanoparticles. NPs-COOH$_{shell}$ (A) −COOH groups were introduced using co-aggregates of Pluronic F127 and a Pluronic F127 dicarboxylic acid derivative as a template. NPs-COOH$_{core}$ (B) −COOH groups were introduced after NP formation, through condensation of CETS into the silica core. In both cases C was used as doping dye and TEOS as silica precursor.

TABLE 1. Morphological and Photophysical Properties of the SiNPs

NPs	[COOH]/[NP]	ζ-potential[a]	[C][b]	brightness[c]	λ_{abs}[d]	λ_{em}[d]	SS[e]	Φ	d_{CORE}[f]	d_H[g] (PDI)[h]
IR813	-	-		3900	815	840	25	0.03	-	-
PEG$_{shell}$	0.0	−4.9 ± 2.0	0.20	8300	830	847	17	0.025	10 ± 2	29 (0.15)
COOH$_{shell}$(2)	2.4	−6.5 ± 1.1	0.20	8000	830	847	17	0.030	10 ± 2	31 (0.20)
COOH$_{shell}$(3)	4.8	−7.0 ± 1.9	0.20	6700	830	847	17	0.025	11.0 ± 2.5	36 (0.13)
COOH$_{shell}$(4)	7.2	−8.8 ± 2.0	0.20	6100	830	847	17	0.020	10 ± 2	68 (0.12)
COOH$_{core}$(2)	4.5	−7.8 ± 0.8	0.12	12 000	830	847	17	0.03	12 ± 2	30 (0.20)
COOH$_{core}$(3)	9.0	−10.8 ± 0.6	0.12	12 000	830	847	17	0.03	12 ± 2	32 (0.16)
COOH$_{core}$(4)	18.0	−14.3 ± 0.8	0.12	13 300	830	847	17	0.04	11 ± 4	45 (0.21)

[a] mV. [b] mg **C**·mL^{-1}. [c] M^{-1} cm^{-1}. [d] nm. [e] Stokes shift, nm. [f] Core diameter (TEM), nm. [g] Hydrodynamic diameter (DLS), nm. [h] Polydispersion index.

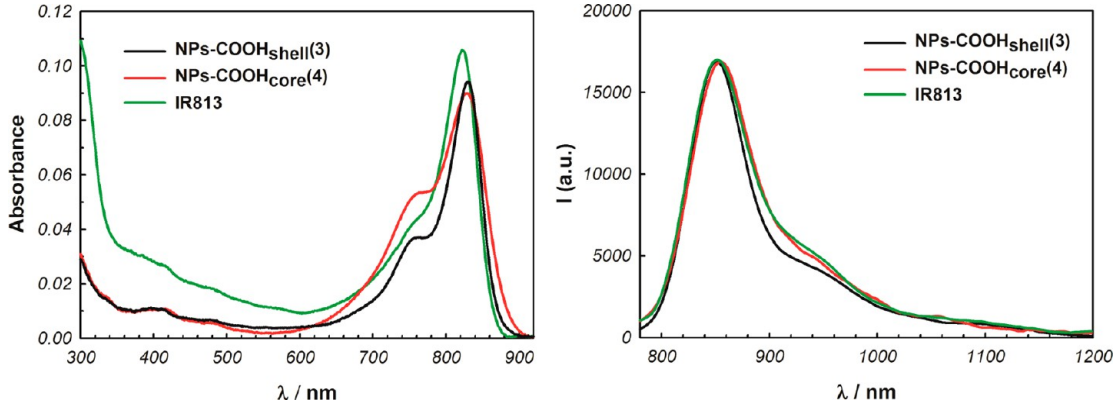

Figure 1. Absorption (left) and emission (right) spectra of dye IR813 (PEG 400/ethanol/water = 3:2:5) and of samples NPs-COOH$_{shell}$(3) and NPs-COOH$_{core}$(4) (water), λ_{ex} = 760 nm.

The dimensions of the silica core (*ca.* 11 nm) are not influenced by the doping material or by the synthetic procedure used (see Table 1 and Figure 2 for examples of NPs-COOH$_{shell}$(i) and NPs-COOH$_{core}$(i)).

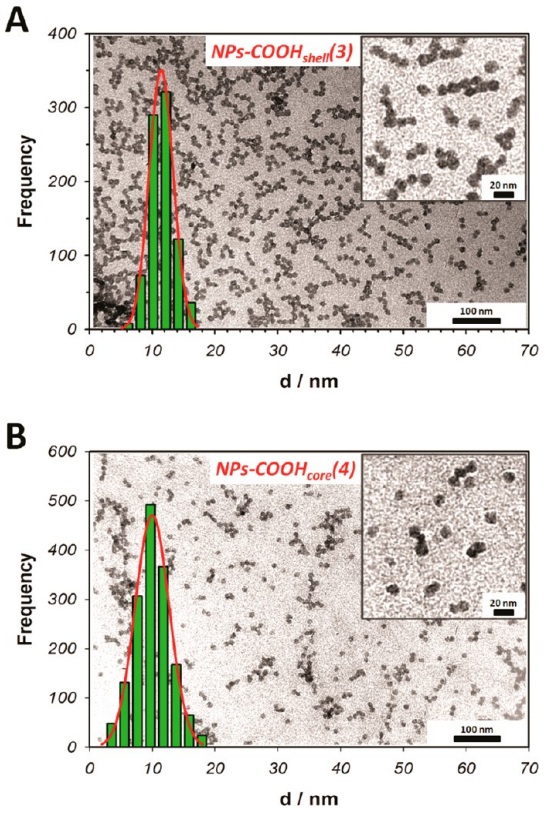

Figure 2. Representative TEM images and silica core size distributions for NPs-COOH$_{shell}$(i) and NPs-COOH$_{core}$(i). (A) NPs-COOH$_{shell}$(3), d = 12 ± 2 nm. (B) NPs-COOH$_{core}$(4), d = (11 ± 2) nm. Insets are taken from higher magnification TEM images, different from the corresponding one in the background.

On the other side, the hydrodynamic diameter in water, while maintaining a rather low polydispersion index (PDI), increases in a nonlinear way upon increasing the amount of inserted carboxylic groups, especially for the NPs-COOH$_{shell}$ family. This behavior is probably imputable to hydrogen bond interactions between the NPs, especially in the samples with higher F127-COOH concentrations. The dynamic nature of these interactions is able to increase the average diameter of the particles but does not affect the colloidal stability of the NP suspensions, thus demonstrating its high stability. To rationalize this phenomenon and to correlate the interaction of different NPs with biological environment, we measured the ζ-potential of the different NP sets (Table 1).

We also estimated the average number of carboxylic groups per particle, considering the NP concentration obtained with this synthetic method,[29] and the different amounts of precursors bearing a carboxylate group introduced during the NP synthesis. As expected, in all cases, the increase in the number of carboxylic groups leads to a decrease of the ζ-potential of the NPs (see Figure 3 and Table 1). The linear decrease of ζ-potential suggests a quantitative incorporation of carboxylate groups that are introduced by means of F127-COOH or CETS during the NP synthesis.

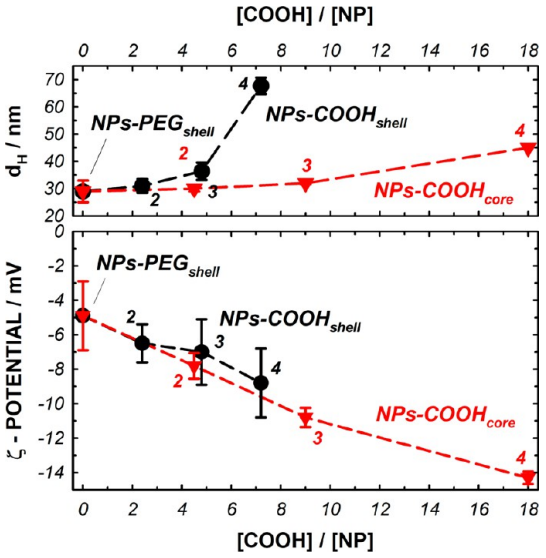

Figure 3. ζ-Potential and hydrodynamic diameter values for NPs-COOHcore(i) and NPs-COOH$_{shell}$(i) samples *versus* the calculated number of carboxylate groups per nanoparticle (conditions: [NPs-COOH] = 2.0 μM; [phosphate buffer] = 1 mM; [KCl] = 1 mM; pH = 7.0; 25 °C; data are mean ± SD (n = 5)).

The NPs-COOH$_{core}$ have a more negative ζ-potential together with a higher degree of control toward NP dimensions and aggregation properties. Therefore these NPs seem to be better adapted for efficient fluorescent lymph node mapping.

***In Vivo* Regional Lymph Node Mapping with Two Families of Cy7-Doped Silica NPs.** After subcutaneous injection of fluorescent tracers in the right anterior paw, the *in vivo* fluorescence signal in the right axillary lymph node was detected at different postinjection times with the modified Fluobeam system (Chart 1). Since the fluorescence signals were normalized to the intensity of the brightest pixel, the injection point where the fluorescence intensity was very strong and as such could interfere with the signal of lymph nodes (see Supporting Information, Figure S16) was hidden, thus enabling a precise localization of the RALN. The fluorescence in the RALN could already be visualized after 5 min whatever the tracer used (Figure 4, upper panel).

The negative surface charge of the tracers could explain their rapid migration into the regional LN, in all probability due to the slight anionic charge of the interstitial matrix, as was proposed earlier for poly(lactic-*co*-glycolic acid) nanoparticles carrying an increasing number of carboxylic groups.[30] A few hours after injection, the free IR813 was extravasated, resulting in a diffuse fluorescent pattern of surrounding tissues (Figure 4E). This result was anticipated considering that an optimal tracers' size should be in the range 10−100 nm.[31,32] Indeed, when 35−45 nm sized **C** doped NPs were injected, the fluorescence was restricted to the LN (Figure 4F, G, H), but NPs-COOH$_{core}$

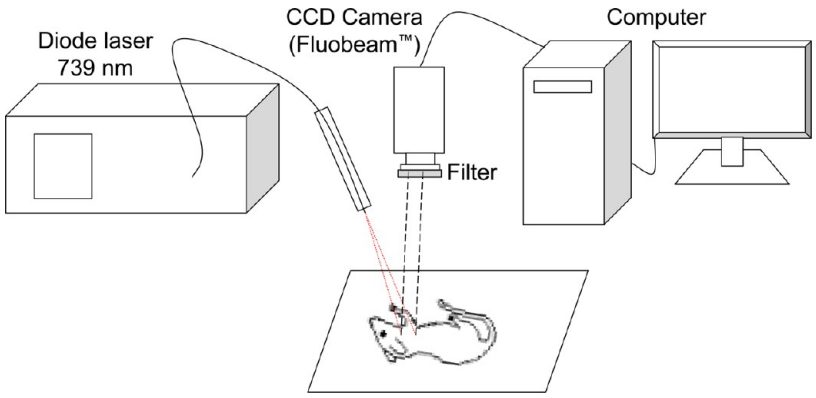

Chart 1. Modified NIR Fluorescence Imaging System

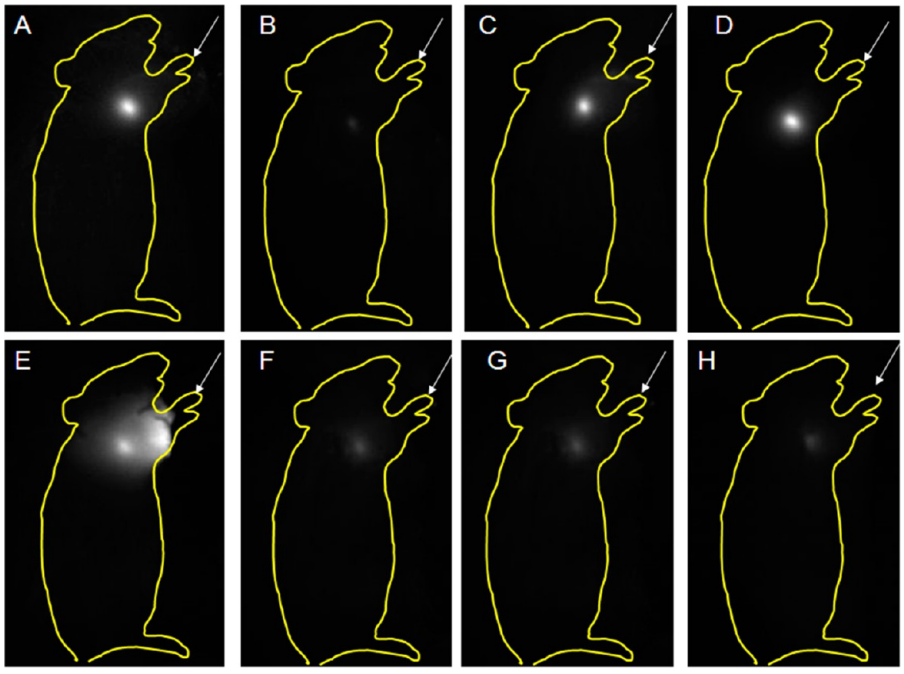

Figure 4. ***In vivo*** **fluorescence imaging of RALN in mice 5 min or 4 h after subcutaneous injection of tracers in the right anterior paw. Mice were subcutaneously injected in the right anterior paw with 5.1 nmol of IR813 dye (20 μL of 0.173 mg/mL IR813 dissolved in a PEG-400/ethanol/water = 3:2:5, v/v/v solution) (A, E), 300 pmol of NPs-COOH$_{shell}$(3) (B, F), 300 pmol of NPs-COOH$_{core}$(2) (C, G), or 300 pmol of NPs-COOH$_{core}$(4) (D, H). Fluorescence imaging of the right flank of mice was performed 5 min (A, B, C, D) or 4 h (E, F, G, H) after injection with a 739 nm excitation light. Injection points (white arrows) were hidden for a better RALN visualization, and exposure time was 10 ms (A, E), 100 ms (D), 200 ms (H), or 300 ms (B, C, F, G); see also Supporting Information Figures S15 and S16.**

and NPs-COOH$_{shell}$ were characterized by strongly different kinetics profiles. NPs-COOH$_{core}$ peaked at 5 min postinjection followed by a rapid exponential decrease (Figure 5 and Figure S17), thus suggesting the rapid detection of RALN during surgery. On the contrary, NPs-COOH$_{shell}$ gradually increased during the first 8 h postadministration with a following decrease until the end of the observation time (Figure 5 and Figure S18). For the sake of comparison, we also present the fluorescence kinetic profile of IR813 (Figure 5), with a maximum fluorescence intensity at 4 h postinjection. Together with a rapid extravasation, the observed accumulation kinetics of IR813 stresses the unfavorable properties of the free dye for LN mapping.

As can be seen from Figure 5, the differences in the kinetic profiles observed within the two sets of NPs are very large and thus of particular interest. We attributed the cause of such differences to a synergy between ζ-potential and size in physiological conditions. To verify this hypothesis, we performed aggregation experiments to observe if the different synthetic strategies could have an effect on the interactions between the NPs and serum proteins (bovine serum albumin, BSA). As can be seen from Figures S13 and S14, NPs-COOH$_{shell}$(i) have an overall higher tendency toward aggregation with BSA compared to NPs-COOH$_{core}$(i), leading to a larger hydrodynamic diameter. If we consider NPs-COOH$_{shell}$(3) and NPs-COOH$_{core}$(2) (Figure 6),

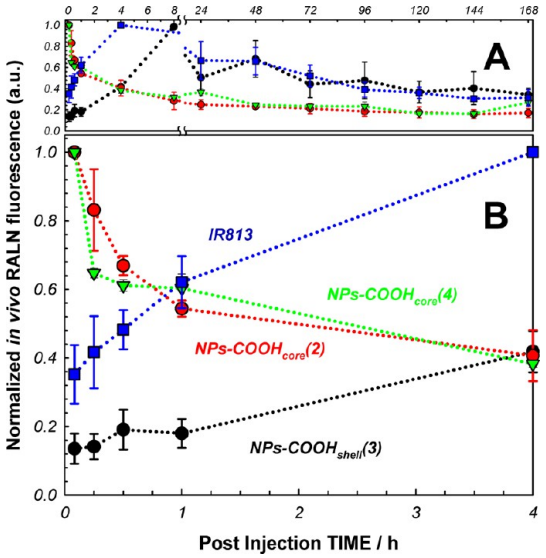

Figure 5. ***In vivo*** **fluorescence intensity of RALN at different postinjection time. Mice were subcutaneously injected in the right anterior paw with 300 pmol of NPs-COOH$_{shell}$(3), NPs-COOH$_{core}$(2), or NPs-COOH$_{core}$(4) and with 5.1 nmol of IR813 dye (20 μL of 0.173 mg/mL IR813 dissolved in a PEG-400/ethanol/water = 3:2:5, v/v/v solution). Fluorescence imaging of RALN was performed at different times after injection with a 739 nm excitation light. (A) Fluorescence kinetics followed for 7 days. (B) Fluorescence kinetics followed for 4 h. Data are mean ± SEM (*n* = 3 per group); see also Supporting Information Figures S17 and S18.**

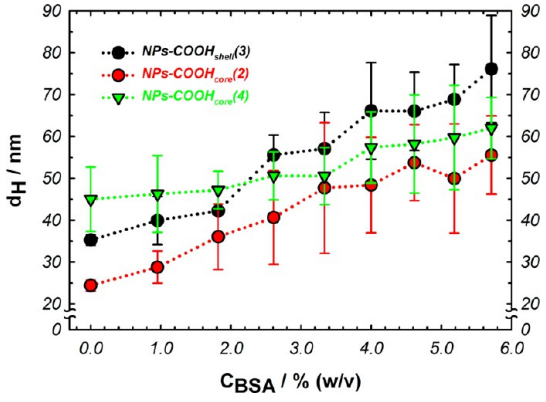

Figure 6. Hydrodynamic diameters (DLS) of NPs-COOH$_{shell}$-(3), NPs-COOH$_{core}$(2), and NPs-COOH$_{core}$(4) in the presence of increasing amounts of BSA (conditions: [NPs] = 8 μM, PBS 1×, 25 °C; pristine NPs and BSA solutions were filtered with an RC 200 nm filter; data are mean ± SD (*n* = 5)).

which have quite similar properties in terms of ζ-potential and hydrodynamic diameter in BSA-free solution, both samples undergo a size increase in the presence of BSA. This is particularly evident considering the physiological concentration for serum proteins (3.4−5.4%, w/v), in which NPs-COOH$_{shell}$(i) present the largest hydrodynamic diameter. The position of the charge, in particular on the surface, is then a major parameter controlling the agglomeration of NPs and the adsorption of proteins, as already reported.[33−35] This finding can explain, at least in part, the faster diffusion in the lymphatic vessels of NPs-COOH$_{core}$, whose hydrodynamic diameter is always less than 60 nm. NPs-COOH$_{core}$(4) prove to be the sample with the best overall performance in RALN mapping, probably because of the more negative ζ-potential and less steep aggregation profile in the presence of BSA. These results clearly indicate that for SLN mapping the NP architecture in which the −COOH groups (necessary to confer a negative ζ-potential) are buried in the PEG shell is more efficient than the one in which the same groups are outstretched from the surface of the NP. It is noteworthy that the versatility of the synthetic procedure can allow tuning in a continuous fashion of the surface charge of the NPs with great accuracy.

Besides favorable photophysical characteristics, NPs-COOH$_{core}$ and in particular NPs-COOH$_{core}$(4) are likely to have an optimal kinetic profile for potential clinical SLN mapping, since regional LN are easily visualized already at 5 min postadministration. Therefore, NPs-COOH$_{core}$(4) were selected for further *in vivo* and *in vitro* experiments.

***In Vitro* and *in Vivo* Toxicity of NPs-COOH$_{core}$.** Assessing nanoparticle toxicity is a prerequisite before *in vivo* administration because several physicochemical properties such as the size, surface charge, particle shape, or NP coating affect their interactions with biological components, thus influencing their toxicity.[36,37] Given their anionic properties, NPs-COOH$_{core}$ are supposed to be nontoxic, compared to cationic particles, which showed a high level of intracellular reactive oxygen species (ROS) production[38] and an increased hemolysis rate.[39] Toxicity studies of NPs-COOH$_{core}$ were conducted *in vitro* in red blood cells (RBC) and fibroblasts and *in vivo* in healthy mice.

The hemolytic capacity is a reference test to study the NPs' interactions with cellular membrane.[40] To this end, RBC were incubated with free IR813 or NPs-COOH$_{core}$ for 2 h, and the hemolytic capacity was further assessed (Figure 7A).

Free IR813 induced a 31.4 ± 3.6% hemolysis at a concentration of 17.3 μM. NPs-COOH$_{core}$ seem to have a protective effect on membrane stability compared to the control RBC since the hemolysis rate of RBC in NP solution (2.6 ± 0.4%) was significantly lower than that in phosphate buffer (8.6 ± 1.1%). PEG-free silica NPs are known to be hemolytic due to the production of ROS[41] and the electrostatic interaction of silanol groups with the trimethyl-ammonium head groups of the RBC membranes.[42] The protective effect of PEGylated NPs could be attributed to the PEG chains, shielding the ROS and the silanol groups.[43]

Another standard assay for *in vitro* toxicity is the MTT test, which informs on the metabolic activity of the cells. Normal human fibroblasts were exposed for 24 h to increasing concentration of free IR813 or NPs (Figure 7B). Already with 5.9 μM IR813 induces 50% cell death, whereas the cells were intact with up to 11.7 μM NPs-COOH$_{core}$. Already 5.9 μM IR813 induces

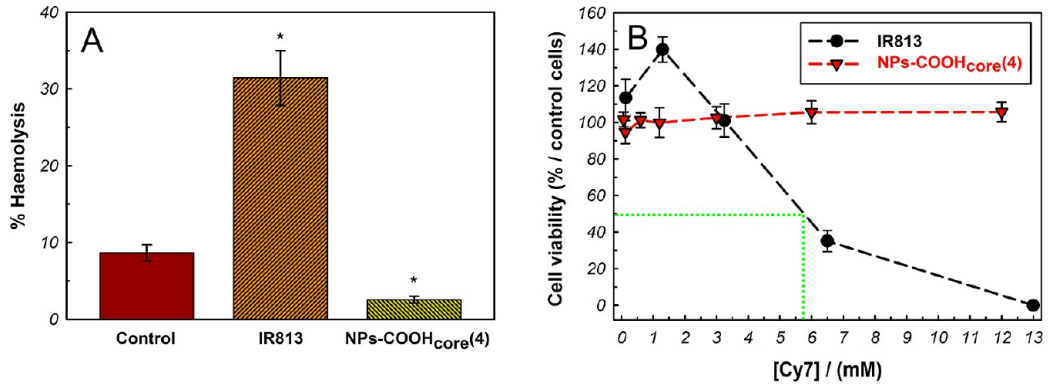

Figure 7. *In vitro* **toxicity of NPs-COOH$_{core}$(4) compared to IR813. (A) Red blood cells were incubated for 2 h with phosphate buffer (control, dark red), 17.3 μM free IR813 (orange, dashed), or 500 nM NPs-COOH$_{core}$(4) (green, dashed). The release of hemoglobin was assessed by the absorbance of the supernatant at 541 nm. Percentage of hemolysis was expressed as the amount of hemoglobin release induced by IR813 or NPs compared to that induced by phosphate buffer. Data are mean $\pm$ SEM (n = 3); hemolysis value marked with an asterisk was significantly different from the control (p < 0.05). (B) Free IR813 (black circles) or NPs-COOH$_{core}$(4) (red triangles) were incubated for 24 h with MRC-5 cells, and the cell viability was assessed by the MTT assay. Green dotted lines correspond to the IC$_{50}$ value for IR813. Data are mean $\pm$ SEM (n = 3).**

50% cell death, whereas the cells were intact with up to 11.7 μM NPs-COOH$_{core}$. An absence of *in vitro* toxicity of NPs-COOH$_{core}$ inspired us to conduct *in vivo* experiments.

The body weight and behavior of mice were recorded for 3 months postinjection. The body weight gain of mice injected with NPs-COOH$_{core}$ was similar to that of control mice (Figure 8A), and no signs of abnormal behavior could be detected. The size of NPs-COOH$_{core}$ is about 40 nm, thus suggesting that hepatobiliary elimination is preferred over that of the kidney.[44] Also, the recent study on the *in vivo* behavior of mesoporous nanoparticles after hypodermic administration demonstrated that, among different organs, a gradual increase in the amount of NPs was observed only in the liver, suggesting that the NPs could cross different biological barriers into the liver.[45] Therefore, we further assessed the functional and morphological hepatic status after subcutaneous injection.

No increase in liver-to-body weight ratios was detected after injection of NPs, thus excluding hepatomegaly (Figure 8B). Functional hepatic activity was assessed by alkaline phosphatase (ALP) serum levels. ALP is a family of enzymes produced by the cells lining the small bile ducts whose serum levels are increased when the biliary drainage system is blocked.[46] At three months postinjection, the ALP serum concentrations of injected mice were identical to those of controls (Figure 8C). Likewise, no morphological changes were observed in mice receiving NPs (Figure 8F,G) compared to control mice (Figure 8D,E). Livers showed no inflammatory responses, and hepatocytes appeared to be normal in all analyzed sections. Lack of *in vitro*[47] and *in vivo* toxicity was already reported with different types of silica NPs.[18,45,48] For QDs the *in vitro* toxicity has been well documented,[33,49−51] while there is no general consensus on the *in vivo* toxicity because observations varied from negligible[52,53] to appreciable toxicity.[50]

Biodistribution of NPs-COOH$_{core}$ in Preclinical Models. Mice were sacrificed at different times after subcutaneous injection of NPs-COOH$_{core}$(4), and organs were *ex vivo* imaged with the modified Fluobeam system. The fluorescence signal at the injection point is maximal until 1 h postinjection and then decreases, with a parallel increase in right lateral thoracic lymph node (RLTLN), liver, and kidney (Figure 9). After 3 months, the fluorescence of organs, except at the injection point and RALN, is similar to those of control organs, indicating their potential elimination. The excretion of NPs-COOH$_{core}$ was assessed by the fluorescence measurement of urine and feces during the first week after injection. Urine was not fluorescent irrespective of the time postinjection (data not shown), whereas feces of mice injected with NPs were highly fluorescent in the first 3 days postinjection, compared to feces of control mice (Figure 10).

The biodistribution of NPs-COOH$_{core}$(4) was close to that obtained with similarly sized indium-based QD, demonstrating a strong accumulation at the injection point and regional lymph nodes with a gradual decrease during the first 3 months.[17] Besides accumulation in the lymphatic system, NPs-COOH$_{core}$(4) were noted in the liver (Figure 9), where they are probably trapped by Kupffer cells.[45] NP transient storage in the liver was also confirmed by ICP-AES silicon analysis (Supporting Infomation), which demonstrated about 20% injected dose (19.3 $\pm$ 5.9% ID) in the liver at 24 h postinjection, while at 3 months follow-up silicon was no longer detectable in the liver (data not shown). A slight but significant increase was also demonstrated in the spleen until 24 h posthypodermic injection, returning to base values after 7 days (Figure 9).

The biodistribution[45] and the size of silica NPs directly affect the excretion route. Whereas small silica

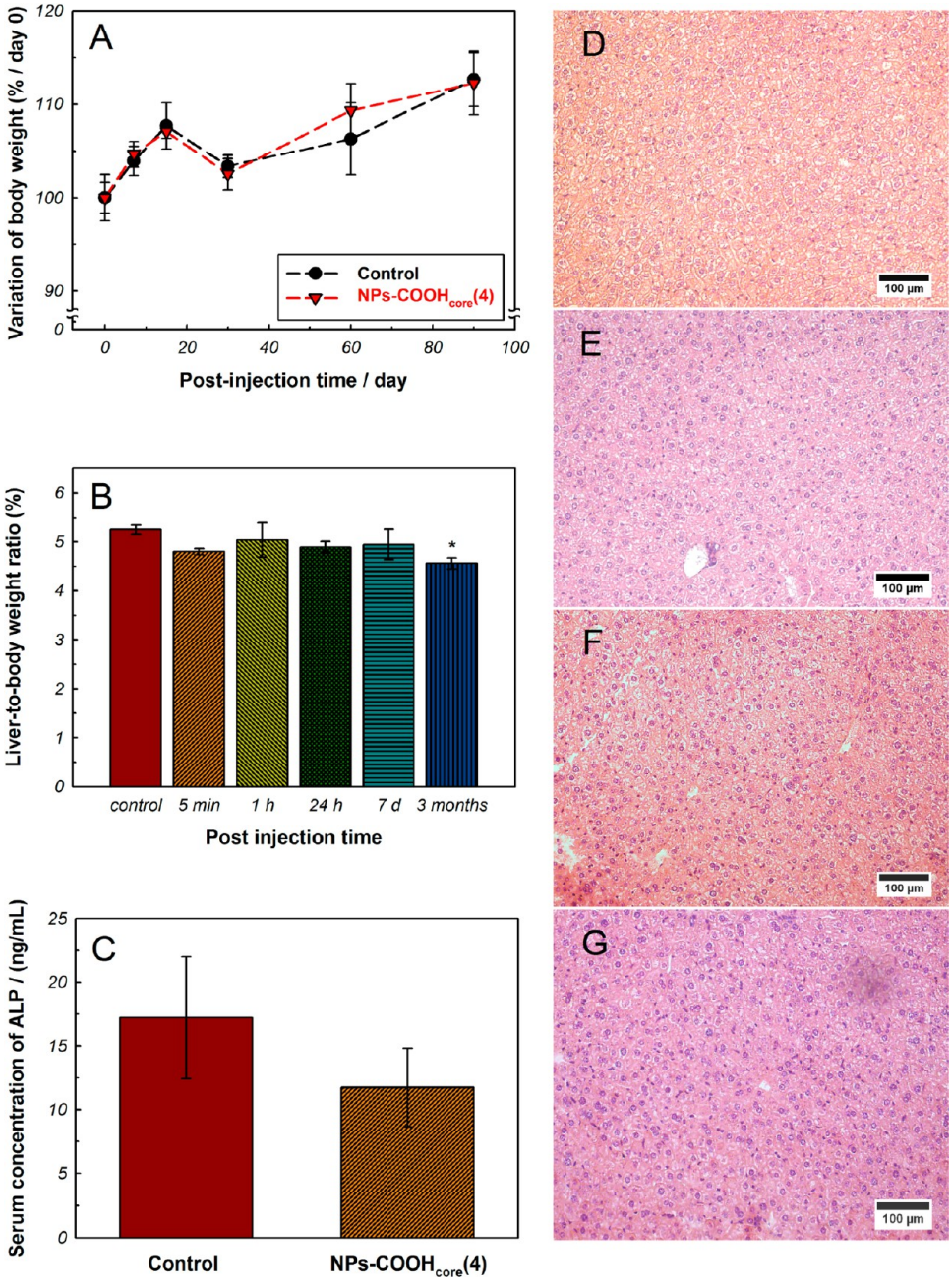

Figure 8. *In vivo* **toxicity of NPs-COOH$_{core}$(4). Mice were subcutaneously injected in the right anterior paw with phosphate buffer (control) or 300 pmol of NPs-COOH$_{core}$(4). The body weights of mice were monitored each week for 3 months and were compared to their starting weight at D0 (A). Mice were sacrificed at different postinjection time (5 min, 1 h, 24 h, 7 days, and 3 months), livers of mice were weighted, and the liver-to-body weight ratios were compared to control mice (B). The serums of mice were collected 3 months after injection, and the serum concentration of alkaline phosphatase (ALP) was compared to control mice (C). (D−G) Representative images of histological sections from the liver of mice 7 days (D, F) or 3 months (E, G) after injection of phosphate buffer (D, E) or NPs-COOH$_{core}$(4) (F, G). Sections were stained with standard HES staining, and images were taken at 10× magnification. Data are mean ± SEM (n = 3); *p < 0.05 compared to control.**

NPs (<6 nm) could be excreted by urine,[54] larger NPs are stored in the liver[55] and cleared *via* feces through the hepatobiliary route.[56,57] The sole observation of urinary excretion of 45 nm silica NPs[58] could be explained by the fact that the fluorophore was not covalently linked to the silica matrix, thus potentially inducing dye leakage and further excretion of free fluorophore, a process that cannot occur in our NPs-COOH. We further assessed the accumulation of NPs in feces for 7 days postinjection. A strong fluorescence signal was observed already 24 h postadministration, followed by progressive elimination during the first 3 days after injection. From the fourth day postadministration the values of fluorescent intensity were not statistically different from control mice (Figure 10).

A broad range of studies on the biodistribution and excretion profiles of SiNPs were conducted

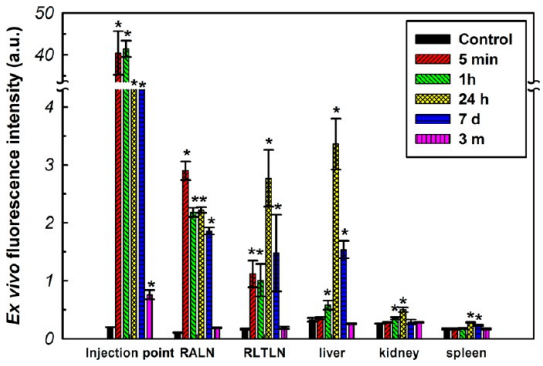

Figure 9. *Ex vivo* fluorescence value of selected organs at different postinjection time. Mice were subcutaneously injected in the right anterior paw with phosphate buffer (control) or 300 pmol of NPs-$COOH_{core}$(4) and were then sacrificed at 5 min, 1 h, 24 h, 7 days, and 3 months after injection. Fluorescence imaging of the injection point, RALN, RLTLN (right lateral thoracic lymph node), liver, kidney, and spleen was performed with a 739 nm excitation light. Data are mean ± SEM (n = 3). Break hidden points: injection point at 24 h is 11.86 ± 0.71 a.u., at 7 d is 7.03 ± 0.39 a.u.; * represents values significantly different from corresponding control organ ($p < 0.05$).

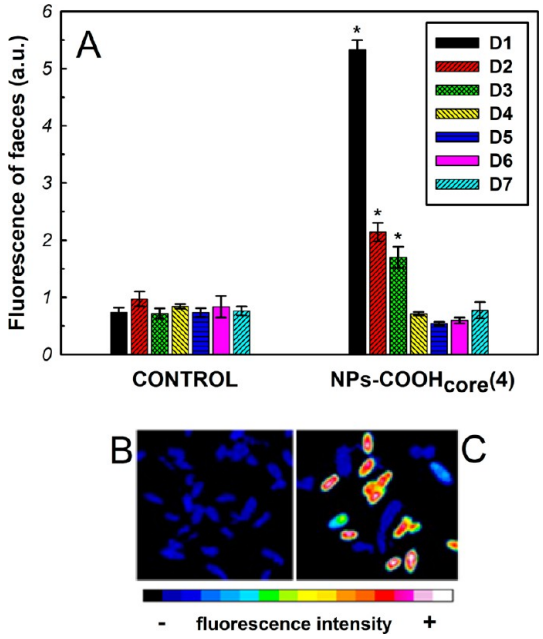

Figure 10. Fluorescence of feces. Mice were subcutaneously injected in the right anterior paw with phosphate buffer (control) or 300 pmol of NPs-$COOH_{core}$(4). Feces were collected daily, and fluorescence signals were assessed with a 739 nm excitation light. (A) Fluorescence intensity of feces as a function of postinjection day. Data are mean ± SEM (n = 3); * represents values significantly different from control feces on the same day ($p < 0.05$). (B, C) Fluorescence images of feces 24 h after injection of phosphate buffer (B) or 300 pmol of NPs-$COOH_{core}$(4) (C), exposure time: 200 ms. False colors were obtained with the 16-color function of ImageJ software.

after intravenous administration,[18,48,59,60] while other exposure routes were less explored.[45,60] The hepatobiliary excretion was documented after iv injection of dye-loaded silica NPs[18,56] evidenced by a fluorescence-guided imaging of NPs in the gastrointestinal tract.[18,52]

TABLE 2. Amounts of Surfactants, Dye, and TEOS Used in NPs-$COOH_{core}$(i) Preparation

NP sample	F127 (mg)	F127-COOH (mg (mmol))	C (mg)	TEOS (μL)	TMSCl (μL)
NPs-$COOH_{shell}$ (1)	100		0.91	175	10
NPs-$COOH_{shell}$ (2)	85	15 (0.0012)	0.91	175	10
NPs-$COOH_{shell}$ (3)	70	30 (0.0024)	0.91	175	10
NPs-$COOH_{shell}$ (4)	55	45 (0.0036)	0.91	175	10

TABLE 3. Amounts of Reagents Used in NPs-$COOH_{core}$(i) Preparation

NP sample	F127 (mg)	C (mg)	TEOS (μL)	CETS (μL (mmol))
NPs-$COOH_{core}$(2)	100	0.94	175	3 (0.0045)
NPs-$COOH_{core}$(3)	100	0.94	175	6 (0.0090)
NPs-$COOH_{core}$(4)	100	0.94	175	12 (0.018)

The recent study by the group of Tang *et al*. examined the behavior of hollow mesoporous SiNPs (*ca*. 110 nm) *in vivo* after the hypodermic exposure route.[45] The biodistribution of SiNPs was qualitatively similar to our data, indicating the liver as a target organ and showing a weak accumulation of NPs in the spleen and kidney. The authors proposed the hepatobiliary excretion of mesoporous silica NPs based on the observation of the increased amount of Si concentration in feces.[45] This finding is consistent with the increase in fluorescence intensity of IR813-doped NPs in fecal masses observed in our study, suggesting hepatobiliary elimination. We would also like to stress that the high chemical stability of these NPs in different conditions (including strong acidic ones) and the covalent link between C and nanoparticle silica core strongly support the excretion of intact nanoparticle and not simply that of NP-dissociated C.

CONCLUSIONS

We designed and synthesized NIR-emitting NPs as efficient probes for *in vivo* mapping of regional lymph nodes in mice. These NPs have a core−shell silica-PEG structure, in which the surface charge (ζ-potential) can be tuned with great accuracy. This synthetic strategy, demonstrating good versatility and reproducibility, can be carried out in mild conditions in water, yielding very stable fluorescent colloidal dispersions. We synthesized two sets of core−shell NPs, covalently doped with the same amount of Cy7 dye (**C**) but differing in terms of the negative charge positioning scheme. Our results clearly show that NP probes in which the negative charges are hidden by a PEG shell outclass similar NP samples possessing external negative charges in terms of fluorescence-guided mapping. These performances strongly depend on the surface characteristics that determine the NPs' colloidal behavior in serum and the biodistribution profile, affecting also the fluorescent intensity kinetic profile. In-depth studies of the NPs'

toxicity, both *in vivo* and *in vitro*, together with a biodistibution profile, suggest the benign nature of these NPs and their efficient excretion by means of a hepatobiliary mechanism. Overall our results demonstrate that the capability to realize silica-based NP probes with a programmable surface charge positioning scheme is of great importance to develop efficient and stable nanoprobes, which are good candidates for RALN mapping in terms of both probing efficiency and nontoxicity.

EXPERIMENTAL SECTION

Materials. Pluronic F127, tetraethyl orthosilicate (TEOS, 99.99%), chlorotrimethylsilane (TMSCl, ≥ 98%), acetic acid (HOAc, ≥ 99.7%), HCl (≥37%), tetrahydrofuran (over molecular sieves, H_2O ≤0.005%, ≥99.5%), 4-(dimethylamino)pyridine (DMAP, ≥ 99%), IR813 perchlorate (80%), 3-aminopropyltriethoxysilane (≥95%), 3-mercaptopropionic acid (≥99%), reagent grade dimethylformamide (DMF), dichloromethane, and acetone were purchased from Sigma-Aldrich. *N,N*-Diisopropylethylamine (DIPEA, ≥ 99.5%), NaCl, and silica on TLC Al foils (4 × 8 cm, with fluorescent indicator 254 nm) were purchased from Fluka. Carboxyethylsilanetriol sodium salt (25% w/w water solution, CETS) was purchesed from GELEST. UF tubes (Amicon Ultra-0.5 mL, cutoff 100 KDa) were purchased from Millipore. Dialysis was performed *versus* water at room temperature under gentle stirring with regenerated cellulose dialysis tubing (Sigma, mol wt cutoff >12 kDa, av diameter 33 mm).

NPs-COOH$_{shell}$ Synthesis. Core−shell silica-PEG (poly(ethylene glycol)) nanoparticles bearing carboxy groups on the PEG surface were synthesized adapting previously reported procedures,[26] using mixtures of Pluronic F127 and Pluronic F127-COOH. Quantities of surfactants and Cy7 dye used are summarized in Table 2. Sample NPs-PEG (x = 0 mg) was used as reference. In a typical preparation 100-x mg of Pluronic F127, x mg of modified F127-COOH, and the amounts of dye shown in Table 2 were carefully solubilized with 1−2 mL of dichloromethane in a 20 mL glass scintillation vial.

The solvent was evaporated from the homogeneous solution by means of a nitrogen flow and subsequently under vacuum at room temperature. NaCl (67 mg) was added to the solid residue, and the mixture was solubilized at 25 °C under magnetic stirring with 1535 μL of 1.0 M acetic acid. TEOS (175 μL, 0.79 mmol) was then added to the resulting aqueous homogeneous solution, followed by TMSCl (10 μL, 0.08 mmol) after 3.0 h. The mixture was kept under stirring for 20 h at 25 °C before dialysis treatments. The dialysis purification steps were carried out *versus* Milli-Q water on a precise amount of nanoparticle solution (1500 μL, RC cutoff 12 kDa, 20 h). The nanoparticles concentration in the dialyzed dispersion diluted to a final volume of 5000 μL was 20 μM, as reported elsewhere.[29]

NPs-COOH$_{core}$ Synthesis. Core−shell silica-PEG nanoparticles with a CETS-doped silica core were synthesized adapting previously reported procedures.[8] The quantities of TEOS, Cy7 dye, and CETS used in the NPs-COOH$_{core}$ synthesis are summarized in Table 3. In a typical preparation 100 mg of Pluronic F127 and the amounts of **C** shown in Table 3 were carefully solubilized with 1−2 mL of dichloromethane in a 20 mL glass scintillation vial.

The solvent was evaporated from the homogeneous solution by means of a nitrogen flow and subsequently under vacuum at room temperature. NaCl (67 mg) was added to the solid residue, and the mixture was solubilized at 25 °C under magnetic stirring with 1535 μL of 1.0 M acetic acid. TEOS (175 μL, 0.79 mmol) was then added to the resulting aqueous homogeneous solution, followed by a suitable amount of CETS after 3.0 h. After an additional 12 h, TMSCl (10 μL, 0.08 mmol) was added, and the mixture was kept under stirring for 20 h at 25 °C before dialysis treatments. The dialysis purification steps were carried out *versus* Milli-Q water on a precise amount of nanoparticles solution (1500 μL, RC cutoff 12 kDa, 20 h). The final concentration of the nanoparticles solution was measured taking into account the volume after the dialysis.[29]

Photophysical Measurements. UV−vis absorption spectra were performed at 25 °C by means of a Perkin-Elmer Lambda 45 spectrophotometer. Quartz cuvettes with an optical path length of 1 cm were used. Corrected fluorescence emission and excitation spectra (450 W Xe lamp) were obtained with an Edinburgh modular UV−vis−NIR spectrofluorimeter, equipped with both a Hamamatsu R928 P photomultiplier tube (for the 500−850 nm spectral range) and an Edinburgh Instruments Ge detector (for the 800−1600 nm spectral range). Corrections for instrumental response, inner filter effects, and phototube sensitivity were performed.[61,62]

The luminescence quantum yields (uncertainty ±15%) of NPs were recorded on air-equilibrated solutions (absorbance <0.1 at the excitation wavelength to avoid autoabsorption), using cyanine IR-125 (ICG, from Acros Organics) in dimethylsulfoxide solution (Φ = 0.13) as reference.[63]

***In Vitro* Toxicity.** *Hemolysis Test.* The method used was reported elsewhere.[42] Briefly, mice blood stabilized with EDTA was obtained by intracardiac puncture before sacrifice. RBC were suspended in phosphate-buffered saline (PBS) (negative control), deionized water (positive control), or increasing dilutions of free IR813 or NPs-COOH$_{core}$ in PBS, ranging from 0 to 17.6 μM IR813 or 0 to 200 nM NPs-COOH$_{core}$ (corresponding to 0−17.3 μM of free dye), respectively. The solutions were incubated for 2 h at 37 °C before centrifugation. The absorbance spectra of the supernatants at 541 nm were measured with a spectrophotometer (Lambda 35, Perkin-Elmer, Courtaboeuf, France). The percentage of hemolysis of each sample was calculated by subtracting the absorption of the negative control from the absorption of the sample, divided by the difference in absorption between positive and negative controls.

Evaluation of Cell Viability. Effects of free IR813 and NPs-COOH$_{core}$ on the viability of MRC-5 cells were evaluated using the MTT assay.[64] Briefly, MRC-5 cells were plated into 96-well plates, and after 24 h the culture medium (RPMI containing 9% inactivated fetal calf serum, 1% penicillin (10 000 UI)−streptomycin (10 000 μg/mL), and 2 mM glutamine) was replaced by 200 μL of free IR813 or NPs-COOH$_{core}$ suspension dissolved in 5% ethanol at concentrations of 0−17.6 μM IR813 or 0−200 nM NPs-COOH$_{core}$ (corresponding to 0−17.3 μM of free dye), respectively. After 24 h, cells were washed, 50 μL of MTT (2 mg/mL) was added to each well, and the plate was incubated at 37 °C for 3 h. The water-insoluble formazan crystals were solubilized with dimethyl sulfoxide (DMSO), and optical density was read on a microplate photometer (Multiskan Ascent, Thermo Labsystems, Finland) at 540 nm.

Animals. The animals received care in accordance with established guidelines of the Federation of European Laboratory Animal Science Associations. Animal procedures were performed in compliance with national guidelines and with approval of the regional ethics committee in animal experiment "Nancy-Lorraine−Nord-Est". All surgery was performed under ketamine/xylazine or isoflurane gaseous anesthesia. Ten-week-old female Balb/cOlaAnN mice (Harlan, Gannat, France) were kept in a 12 h light/dark cycle and had access to food and water *ad libitum*. A specific purified diet (TD.94045, Harlan Teklad, Madison, WI, USA) was used to reduce tissue autofluorescence in the NIR region. Mice were housed in a metabolism cage to collect daily excretions.

Near-Infrared Fluorescence Imaging. *In vivo* optical imaging of fluorescent dye was performed using the Fluobeam700 NIR imaging system (Fluoptics, Grenoble, France) coupled with a 739-nm-emitting laser diode (Biolitec AG, Jena, Germany) (Chart 1).

A 750 nm long-pass emission cutoff filter was added to the highly sensitive Fluobeam charge-coupled device camera for gathering of fluorescence. The power of the diode was fixed to 100 mW, resulting in a power of 3.5 mW at 15 cm from the fiber exit. Semiquantitative data were obtained from the fluorescence images using ImageJ 1.44 software. A segmentation protocol

(max entropy method) was applied to threshold the images for each organ. The CCD camera of the Fluobeam system adjusts the contrast of the image according to the intensity of the brightest pixel. Fluorescent signals were expressed in arbitrary units (a.u.) as the mean intensity of pixels of the threshold organ.

Visualization of Axillary Lymph Node. Mice were subcutaneously (sc) injected in the distal part of the right anterior paw with 20 μL of either physiological solution or 5.1 nmol of free IR813 dissolved in a PEG-400/ethanol/water (3:2:5, v/v/v) solution or 15 μM NPs-$COOH_{core}$ suspension (corresponding to 5.1 nmol of free dye). The fluorescence intensity in the axillary lymph node (ALN) was recorded for 1 week using the imaging system described before. The injection point was hidden during RALN imaging.

Biodistribution Study. Seven groups of animals (n = 6 per group) were used for the biodistribution study: one control group received PBS and was sacrificed 7 days after injection, and six experimental groups, where animals were injected with NPs-$COOH_{core}$, were sacrificed at 5 min, 1 h, 4 h, 24 h, 7 days, and 3 months after injection. Mice were sc injected in the distal part of the right anterior paw with 20 μL of PBS or 20 μL of a 15 μM NPs-$COOH_{core}$ solution (300 pmol), and the paw was kneaded to improve product migration. After sacrifice, organs, axillary lymph nodes (ALNs), lateral thoracic lymph nodes (LTLNs), brain, bladder, intestine, spleen, pancreas, stomach, kidneys, liver, heart, lungs, and injection point) were removed, weighed, and imaged using the imaging system described before. Organs of interest (ALN, injection point, liver, and feces) were frozen prior to silicon elemental analysis.

***In Vivo* Toxicity.** Animals were weighed and observed daily for any weight loss or behavioral abnormalities. The liver-to-body weight ratio was calculated at each time postinjection to evaluate the liver toxicity. The alkaline phosphatase activity in serum was performed with SensoLyte pNPP alkaline phosphatase assay kit (Anaspec, Fremont, CA, USA) in accordance with the supplier instructions. Blood samples were collected through cardiac puncture in BD Vacutainer SST II Advance tubes with clot activator and gel for serum separation (Becton Dickinson, Le-Pont-de-Claix, France) before sacrifice. The concentration of alkaline phosphatase in serum samples was calculated from their absorption at 405 nm (Lambda 35, Perkin-Elmer, Courtaboeuf, France) after 20 min of incubation with pNPP substrate solution.

Livers were harvested at different postinjection times and fixed in AFA (alcohol formalin and acetic acid) before being embedded in paraffin, cut in 5-μm-thick sections, and stained with hematoxylin, eosin, and saffron (HES). The histological sections were observed under an optical microscope and compared to those of control mice.

Statistical Analysis. Means and standard errors of the mean (SEM) were determined using standard software; statistical significance between groups (Mann−Whitney test) was calculated with StatView software (SAS Institute Inc., Cary, NC, USA); p values of <0.05 were considered statistically significant.

Conflict of Interest: The authors declare no competing financial interest.

Supporting Information Available: Synthesis and characterization of organic compounds and nanoparticle characterization (TEM images, DLS measurements, *in vivo* RALN fluorescence, ICP-AES technique). This material is available free of charge *via* the Internet at http://pubs.acs.org.

Acknowledgment. We thank the Ligue Nationale contre le Cancer, the Lorraine Region and the Institut de Cancérologie de Lorraine, and the Italian Ministry for University and Research MIUR (PRIN 2009Z9ASCA and PON 01_01078 projects) for their funding.

Note Added after ASAP Publication: This paper was published ASAP on September 26, 2013. There were numerous corrections in Table 1, Scheme 1 and Abstract graphic, and text changes throughout the manuscript. The corrected version was reposted on September 30, 2013.

REFERENCES AND NOTES

1. Kobayashi, H.; Koyama, Y.; Barrett, T.; Hama, Y.; Regino, C. A.; Shin, I. S.; Jang, B. S.; Le, N.; Paik, C. H.; Choyke, P. L.; *et al*. Multimodal Nanoprobes for Radionuclide and Five-Color near-Infrared Optical Lymphatic Imaging. *ACS Nano* **2007**, *1*, 258–264.
2. Voura, E. B.; Jaiswal, J. K.; Mattoussi, H.; Simon, S. M. Tracking Metastatic Tumor Cell Extravasation with Quantum Dot Nanocrystals and Fluorescence Emission-Scanning Microscopy. *Nat. Med.* **2004**, *10*, 993–998.
3. Smith, J. D.; Fisher, G. W.; Waggoner, A. S.; Campbell, P. G. The Use of Quantum Dots for Analysis of Chick Cam Vasculature. *Microvasc. Res.* **2007**, *73*, 75–83.
4. Akerman, M. E.; Chan, W. C.; Laakkonen, P.; Bhatia, S. N.; Ruoslahti, E. Nanocrystal Targeting *in Vivo*. *Proc. Natl. Acad. Sci. U.S.A.* **2002**, *99*, 12617–12621.
5. Burns, A.; Sengupta, P.; Zedayko, T.; Baird, B.; Wiesner, U. Core/Shell Fluorescent Silica Nanoparticles for Chemical Sensing: Towards Single-Particle Laboratories. *Small* **2006**, *2*, 723–726.
6. Burns, A.; Ow, H.; Wiesner, U. Fluorescent Core-Shell Silica Nanoparticles: Towards "Lab on a Particle" Architectures for Nanobiotechnology. *Chem. Soc. Rev.* **2006**, *35*, 1028–1042.
7. Kumar, R.; Roy, I.; Ohulchanskyy, T. Y.; Goswami, L. N.; Bonoiu, A. C.; Bergey, E. J.; Tramposch, K. M.; Maitra, A.; Prasad, P. N. Covalently Dye-Linked, Surface-Controlled, and Bioconjugated Organically Modified Silica Nanoparticles as Targeted Probes for Optical Imaging. *ACS Nano* **2008**, *2*, 449–456.
8. Rampazzo, E.; Boschi, F.; Bonacchi, S.; Juris, R.; Montalti, M.; Zaccheroni, N.; Prodi, L.; Calderan, L.; Rossi, B.; Becchi, S. *et al*. Multicolor Core/Shell Silica Nanoparticles for *in Vivo* and *ex Vivo* Imaging. *Nanoscale* **2012**, *4*, 824–830.
9. Wang, L.; Wang, K.; Santra, S.; Zhao, X.; Hilliard, L. R.; Smith, J. E.; Wu, Y.; Tan, W. Watching Silica Nanoparticles Glow in the Biological World. *Anal. Chem.* **2006**, *78*, 646–654.
10. Weissleder, R.; Ntziachristos, V. Shedding Light onto Live Molecular Targets. *Nat. Med.* **2003**, *9*, 123–128.
11. Tanaka, E.; Choi, H. S.; Fujii, H.; Bawendi, M. G.; Frangioni, J. V. Image-Guided Oncologic Surgery Using Invisible Light: Completed Pre-Clinical Development for Sentinel Lymph Node Mapping. *Ann. Surg. Oncol.* **2006**, *13*, 1671–1681.
12. Tellier, F.; Steibel, J.; Chabrier, R.; Ble, F. X.; Tubaldo, H.; Rasata, R.; Chambron, J.; Duportail, G.; Simon, H.; Rodier, J. F.; *et al*. Sentinel Lymph Nodes Fluorescence Detection and Imaging Using Patent Blue V Bound to Human Serum Albumin. *Biomed. Opt. Express* **2012**, *3*, 2306–2316.
13. Erogbogbo, F.; Yong, K.-T.; Roy, I.; Hu, R.; Law, W.-C.; Zhao, W.; Ding, H.; Wu, F.; Kumar, R.; Swihart, M. T.; *et al*. *In Vivo* Targeted Cancer Imaging, Sentinel Lymph Node Mapping and Multi-Channel Imaging with Biocompatible Silicon Nanocrystals. *ACS Nano* **2010**, *5*, 413–423.
14. Kim, S.; Lim, Y. T.; Soltesz, E. G.; De Grand, A. M.; Lee, J.; Nakayama, A.; Parker, J. A.; Mihaljevic, T.; Laurence, R. G.; Dor, D. M.; *et al*. Near-Infrared Fluorescent Type II Quantum Dots for Sentinel Lymph Node Mapping. *Nat. Biotechnol.* **2004**, *22*, 93–97.
15. Troyan, S. L.; Kianzad, V.; Gibbs-Strauss, S. L.; Gioux, S.; Matsui, A.; Oketokoun, R.; Ngo, L.; Khamene, A.; Azar, F.; Frangioni, J. V. The Flare Intraoperative near-Infrared Fluorescence Imaging System: A First-in-Human Clinical Trial in Breast Cancer Sentinel Lymph Node Mapping. *Ann. Surg. Oncol.* **2009**, *16*, 2943–2952.
16. Pons, T.; Pic, E.; Lequeux, N.; Cassette, E.; Bezdetnaya, L.; Guillemin, F.; Marchal, F.; Dubertret, B. Cadmium-Free Cuins2/Zns Quantum Dots for Sentinel Lymph Node Imaging with Reduced Toxicity. *ACS Nano* **2010**, *4*, 2531–2538.
17. Helle, M.; Cassette, E.; Bezdetnaya, L.; Pons, T.; Leroux, A.; Plenat, F.; Guillemin, F.; Dubertret, B.; Marchal, F. Visualisation of Sentinel Lymph Node with Indium-Based near Infrared Emitting Quantum Dots in a Murine Metastatic Breast Cancer Model. *PLoS One* **2012**, *7*, e44433.
18. Kumar, R.; Roy, I.; Ohulchanskky, T. Y.; Vathy, L. A.; Bergey, E. J.; Sajjad, M.; Prasad, P. N. *In Vivo* Biodistribution and Clearance Studies Using Multimodal Organically Modified Silica Nanoparticles. *ACS Nano* **2010**, *4*, 699–708.

19. Bonacchi, S.; Genovese, D.; Juris, R.; Montalti, M.; Prodi, L.; Rampazzo, E.; Zaccheroni, N. Luminescent Silica Nanoparticles: Extending the Frontiers of Brightness. *Angew. Chem., Int. Ed.* **2011**, *50*, 4056–4066.
20. Kim, S.; Ohulchanskyy, T. Y.; Bharali, D.; Chen, Y.; Pandey, R. K.; Prasad, P. N. Organically Modified Silica Nanoparticles with Intraparticle Heavy-Atom Effect on the Encapsulated Photosensitizer for Enhanced Efficacy of Photodynamic Therapy. *J. Phys. Chem. C* **2009**, *113*, 12641–12644.
21. Medley, C. D.; Bamrungsap, S.; Tan, W.; Smith, J. E. Aptamer-Conjugated Nanoparticles for Cancer Cell Detection. *Anal. Chem.* **2011**, *83*, 727–734.
22. Wang, L.; Zhao, W.; O'Donoghu, M. B.; Tan, W. Fluorescent Nanoparticles for Multiplexed Bacteria Monitoring. *Bioconjugate Chem.* **2007**, *18*, 297–301.
23. Piao, Y.; Burns, A.; Kim, J.; Wiesner, U.; Hyeon, T. Designed Fabrication of Silica-Based Nanostructured Particle Systems for Nanomedicine Applications. *Adv. Funct. Mater.* **2008**, *18*, 3745–3758.
24. Ma, K.; Sai, H.; Wiesner, U. Ultrasmall Sub-10 nm near-Infrared Fluorescent Mesoporous Silica Nanoparticles. *J. Am. Chem. Soc.* **2012**, *134*, 13180–13183.
25. Tang, L.; Yang, X.; Dobrucki, L. W.; Chaudhury, I.; Yin, Q.; Yao, C.; Lezmi, S.; Helferich, W. G.; Fan, T. M.; Cheng, J. Aptamer-Functionalized, Ultra-Small, Monodisperse Silica Nanoconjugates for Targeted Dual-Modal Imaging of Lymph Nodes with Metastatic Tumors. *Angew. Chem., Int. Ed.* **2012**, *51*, 12721–12726.
26. Soster, M.; Juris, R.; Bonacchi, S.; Genovese, D.; Montalti, M.; Rampazzo, E.; Zaccheroni, N.; Garagnani, P.; Bussolino, F.; Prodi, L.; *et al*. Targeted Dual-Color Silica Nanoparticles Provide Univocal Identification of Micrometastases in Preclinical Models of Colorectal Cancer. *Int. J. Nanomed.* **2012**, *7*, 4797–4807.
27. Wang, X.-d.; Stolwijk, J. A.; Lang, T.; Sperber, M.; Meier, R. J.; Wegener, J.; Wolfbeis, O. S. Ultra-Small, Highly Stable, and Sensitive Dual Nanosensors for Imaging Intracellular Oxygen and pH in Cytosol. *J. Am. Chem. Soc.* **2012**, *134*, 17011–17014.
28. Quan, B.; Choi, K.; Kim, Y. H.; Kang, K. W.; Chung, D. S. Near Infrared Dye Indocyanine Green Doped Silica Nanoparticles for Biological Imaging. *Talanta* **2012**, *99*, 387–393.
29. Rampazzo, E.; Bonacchi, S.; Juris, R.; Montalti, M.; Genovese, D.; Zaccheroni, N.; Prodi, L.; Rambaldi, D. C.; Zattoni, A.; Reschiglian, P. Energy Transfer from Silica Core−Surfactant Shell Nanoparticles to Hosted Molecular Fluorophores. *J. Phys. Chem. B* **2010**, *114*, 14605–14613.
30. Buckle, T.; Chin, P. T.; van Leeuwen, F. W. (Non-Targeted) Radioactive/Fluorescent Nanoparticles and Their Potential in Combined Pre- and Intraoperative Imaging during Sentinel Lymph Node Resection. *Nanotechnology* **2010**, *21*, 482001.
31. Zimmer, J. P.; Kim, S. W.; Ohnishi, S.; Tanaka, E.; Frangioni, J. V.; Bawendi, M. G. Size Series of Small Indium Arsenide-Zinc Selenide Core-Shell Nanocrystals and Their Application to *in Vivo* Imaging. *J. Am. Chem. Soc.* **2006**, *128*, 2526–2527.
32. Uren, R. F.; Howman-Giles, R. B.; Thompson, J. F. Regarding Sentinel Lymph Node Localization in Early Breast Cancer. *J. Nucl. Med.* **1999**, *40*, 1403–1406.
33. Hoshino, A.; Fujioka, K.; Oku, T.; Suga, M.; Sasaki, Y. F.; Ohta, T.; Yasuhara, M.; Suzuki, K.; Yamamoto, K. Physicochemical Properties and Cellular Toxicity of Nanocrystal Quantum Dots Depend on Their Surface Modification. *Nano Lett.* **2004**, *4*, 2163–2169.
34. Monopoli, M. P.; Aberg, C.; Salvati, A.; Dawson, K. A. Biomolecular Coronas Provide the Biological Identity of Nanosized Materials. *Nat. Nanotechnol.* **2012**, *7*, 779–786.
35. Rocker, C.; Potzl, M.; Zhang, F.; Parak, W. J.; Nienhaus, G. U. A Quantitative Fluorescence Study of Protein Monolayer Formation on Colloidal Nanoparticles. *Nat. Nanotechnol.* **2009**, *4*, 577–580.
36. Sharifi, S.; Behzadi, S.; Laurent, S.; Laird Forrest, M.; Stroeve, P.; Mahmoudi, M. Toxicity of Nanomaterials. *Chem. Soc. Rev.* **2012**, *41*, 2323–2343.
37. Sohaebuddin, S.; Thevenot, P.; Baker, D.; Eaton, J.; Tang, L. Nanomaterial Cytotoxicity Is Composition, Size, and Cell Type Dependent. *Part. Fibre Toxicol.* **2010**, *7*, 22.
38. Bhattacharjee, S.; de Haan, L.; Evers, N.; Jiang, X.; Marcelis, A.; Zuilhof, H.; Rietjens, I.; Alink, G. Role of Surface Charge and Oxidative Stress in Cytotoxicity of Organic Monolayer-Coated Silicon Nanoparticles towards Macrophage Nr8383 Cells. *Part. Fibre Toxicol.* **2010**, *7*, 25.
39. Goodman, C. M.; McCusker, C. D.; Yilmaz, T.; Rotello, V. M. Toxicity of Gold Nanoparticles Functionalized with Cationic and Anionic Side Chains. *Bioconjugate Chem.* **2004**, *15*, 897–900.
40. Chouly, C.; Bordenave, L.; Bareille, R.; Guerin, V.; Baquey, A.; Pouliquen, D.; Baquey, C.; Jallet, P. *In Vitro* Study of the Hemocompatibility of Superparamagnetic Contrast Agent for Magnetic Resonance Imaging. *Clin. Mater.* **1994**, *15*, 293–301.
41. Nash, T.; Allison, A. C.; Harington, J. S. Physico-Chemical Properties of Silica in Relation to Its Toxicity. *Nature* **1966**, *210*, 259–261.
42. Slowing, I.; Wu, C. W.; Vivero-Escoto, J. L.; Lin, V. S. Mesoporous Silica Nanoparticles for Reducing Hemolytic Activity Towards Mammalian Red Blood Cells. *Small* **2009**, *5*, 57–62.
43. He, Q.; Zhang, J.; Shi, J.; Zhu, Z.; Zhang, L.; Bu, W.; Guo, L.; Chen, Y. The Effect of Pegylation of Mesoporous Silica Nanoparticles on Nonspecific Binding of Serum Proteins and Cellular Responses. *Biomaterials* **2010**, *31*, 1085–1092.
44. Longmire, M.; Choyke, P. L.; Kobayashi, H. Clearance Properties of Nano-Sized Particles and Molecules as Imaging Agents: Considerations and Caveats. *Nanomedicine (London, U. K.)* **2008**, *3*, 703–717.
45. Fu, C.; Liu, T.; Li, L.; Liu, H.; Chen, D.; Tang, F. The Absorption, Distribution, Excretion and Toxicity of Mesoporous Silica Nanoparticles in Mice Following Different Exposure Routes. *Biomaterials* **2013**, *34*, 2565–2575.
46. Patlolla, A. K.; Berry, A.; Tchounwou, P. B. Study of Hepatotoxicity and Oxidative Stress in Male Swiss-Webster Mice Exposed to Functionalized Multi-Walled Carbon Nanotubes. *Mol. Cell. Biochem.* **2011**, *358*, 189–199.
47. Rampazzo, E.; Voltan, R.; Petrizza, L.; Zaccheroni, N.; Prodi, L.; Casciano, F.; Zauli, G.; Secchiero, P. Proper Design of Silica Nanoparticles Combines High Brightness, Lack of Cytotoxicity and Efficient Cell Endocytosis. *Nanoscale* **2013**, *5*, 7897–7905.
48. Huang, X.; Li, L.; Liu, T.; Hao, N.; Liu, H.; Chen, D.; Tang, F. The Shape Effect of Mesoporous Silica Nanoparticles on Biodistribution, Clearance, and Biocompatibility *in Vivo*. *ACS Nano* **2011**, *5*, 5390–5399.
49. Shiohara, A.; Hoshino, A.; Hanaki, K.; Suzuki, K.; Yamamoto, K. On the Cyto-Toxicity Caused by Quantum Dots. *Microbiol. Immunol.* **2004**, *48*, 669–675.
50. Zhang, Y.; Chen, W.; Zhang, J.; Liu, J.; Chen, G.; Pope, C. *In Vitro* and *in Vivo* Toxicity of CdTe Nanoparticles. *J. Nanosci. Nanotechnol.* **2007**, *7*, 497–503.
51. Geys, J.; Nemmar, A.; Verbeken, E.; Smolders, E.; Ratoi, M.; Hoylaerts, M. F.; Nemery, B.; Hoet, P. H. M. Acute Toxicity and Prothrombotic Effects of Quantum Dots: Impact of Surface Charge *Environ*. *Health Perspect.* **2008**, *116*, 1607–1613.
52. Hauck, T. S.; Anderson, R. E.; Fischer, H. C.; Newbigging, S.; Chan, W. C. W. *In Vivo* Quantum-Dot Toxicity Assessment. *Small* **2010**, *6*, 138–144.
53. Ye, L.; Yong, K.-T.; Liu, L.; Roy, I.; Hu, R.; Zhu, J.; Cai, H.; Law, W.-C.; Liu, J.; Wang, K.; *et al*. A Pilot Study in Non-Human Primates Shows No Adverse Response to Intravenous Injection of Quantum Dots. *Nat. Nanotechnol.* **2012**, *7*, 453–458.
54. Burns, A. A.; Vider, J.; Ow, H.; Herz, E.; Penate-Medina, O.; Baumgart, M.; Larson, S. M.; Wiesner, U.; Bradbury, M. Fluorescent Silica Nanoparticles with Efficient Urinary Excretion for Nanomedicine. *Nano Lett.* **2009**, *9*, 442–448.
55. Lee, C.-H.; Cheng, S.-H.; Wang, Y.-J.; Chen, Y.-C.; Chen, N.-T.; Souris, J.; Chen, C.-T.; Mou, C.-Y.; Yang, C.-S.; Lo, L.-W.

Near-Infrared Mesoporous Silica Nanoparticles for Optical Imaging: Characterization and *in Vivo* Biodistribution. *Adv. Funct. Mater.* **2009**, *19*, 215–222.
56. Souris, J. S.; Lee, C. H.; Cheng, S. H.; Chen, C. T.; Yang, C. S.; Ho, J. A.; Mou, C. Y.; Lo, L. W. Surface Charge-Mediated Rapid Hepatobiliary Excretion of Mesoporous Silica Nanoparticles. *Biomaterials* **2010**, *31*, 5564–5574.
57. Yu, T.; Hubbard, D.; Ray, A.; Ghandehari, H. *In Vivo* Biodistribution and Pharmacokinetics of Silica Nanoparticles as a Function of Geometry, Porosity and Surface Characteristics. *J. Controlled Release* **2012**, *163*, 46–54.
58. He, X.; Nie, H.; Wang, K.; Tan, W.; Wu, X.; Zhang, P. *In Vivo* Study of Biodistribution and Urinary Excretion of Surface-Modified Silica Nanoparticles. *Anal. Chem.* **2008**, *80*, 9597–9603.
59. Liu, T.; Li, L.; Teng, X.; Huang, X.; Liu, H.; Chen, D.; Ren, J.; He, J.; Tang, F. Single and Repeated Dose Toxicity of Mesoporous Hollow Silica Nanoparticles in Intravenously Exposed Mice. *Biomaterials* **2011**, *32*, 1657–1668.
60. Jaganathan, H.; Godin, B. Biocompatibility Assessment of Si-Based Nano- and Micro-Particles. *Adv. Drug Delivery Rev.* **2012**, *64*, 1800–1819.
61. Credi, A.; Prodi, L. From Observed to Corrected Luminescence Intensity of Solution Systems: An Easy-to-Apply Correction Method for Standard Spectrofluorimeters. *Spectrochim. Acta, Part A* **1998**, *54*, 159–170.
62. Montalti, M.; Credi, A.; Prodi, L.; Gandolfi, M. T. *Handbook of Photochemistry*, 3rd ed.; CRC Taylor & Francis: Boca Raton, FL, 2006.
63. Soper, S. A.; Mattingly, Q. L. Steady-State and Picosecond Laser Fluorescence Studies of Nonradiative Pathways in Tricarbocyanine Dyes: Implications to the Design of near-IR Fluorochromes with High Fluorescence Efficiencies. *J. Am. Chem. Soc.* **1994**, *116*, 3744–3752.
64. Levitz, S. M.; Diamond, R. D. A Rapid Colorimetric Assay of Fungal Viability with the Tetrazolium Salt MTT. *J. Infect. Dis.* **1985**, *152*, 938–945.